Title
Radiation Tolerant Interface Design and Complexion Dynamics via Atomistic Modeling

Author
Ludy, Joseph Earl

Publication Date
2016

Peer reviewed|Thesis/dissertation

UNIVERSITY OF CALIFORNIA,
IRVINE

Radiation Tolerant Interface Design and Complexion Dynamics via Atomistic Modeling

THESIS

submitted in partial satisfaction of the requirements
for the degree of

MASTER OF SCIENCE

in Mechanical and Aerospace Engineering

by

Joseph Earl Ludy

Thesis Committee:
Assistant Professor Timothy Rupert, Chair
Associate Professor Lorenzo Valdevit
Associate Professor Manuel Gamero-Castaño

2016

DEDICATION

To

my mother and father

for their love and support with all of my endeavors.

Table of Contents

Page

List of Figures

Page

Acknowledgements

I would like to thank everyone at UCI who has helped me throughout my graduate career.

Abstract of the Thesis

Radiation Tolerant Interface Design and Complexion Dynamics via Atomistic Modeling

By

Joseph Earl Ludy

Master of Science in Mechanical and Aerospace Engineering

University of California, Irvine, 2016

Assistant Professor Timothy Rupert, Chair

Traditionally, grain boundary character in nanoscale materials has been tailored to maximize different types of mechanical behavior, whether it be exhibiting near-theoretical strengths or prolonging fracture by dramatically increasing a material's ductility. As more complex systems develop for nuclear and other extreme environment applications, the need for these types of materials is quickly identified. Specifically, materials in a nuclear reactor need to be amended to extend their longevity to promote safety and reliable usage. One strategy for improving radiation tolerance is the design and control of internal interfaces in a material. Atomistic simulations can give insight into the foundational principles of grain boundary structure and formation.

Two comprehensive simulation models are developed to bridge this gap with respect to radiation tolerant interfaces and structural transitions in binary alloy systems. Firstly, the radiation damage of an ordered grain boundary is compared to a disordered amorphous intergranular film, to investigate how interface thickness and free volume impacts point defect recombination. Collision cascades are simulated and residual point defect populations are analyzed as a function of boundary type and primary knock on atom energy. Secondly, hybrid

Monte Carlo/molecular dynamics simulations are used to study segregation-induced intergranular film formation in Cu-Zr and Cu-Nb alloys. While Cu-Zr alloys form structurally disordered or amorphous films, second phases precipitate at the interfaces of Cu-Nb. Finally, the effect of free surfaces on dopant segregation and complexion formation is investigated for both alloys.

Chapter 1: Introduction

1.1 Grain Boundary Engineering

1.1.1 Background

Grain boundaries (GBs) are the interfaces between two grains or crystallites in a polycrystalline material. GBs in polycrystalline metals can be sources of strength or weakness due to their ability to act as mobile dislocation sinks. Since GB structure is less rigid than the lattice, this can lead to intergranular fracture [1]. However, their open structure can also accommodate strain as GBs are barriers to mechanical slip [2]. This accommodation can be explained by the idea of excess free volume. Free volume within a boundary is created by the breakdown of crystalline structure at the GB [3]. GBs do not adhere to any specific crystalline type and represent a break in the lattice structure. Therefore, to mitigate intergranular cracking and other failure mechanisms, the interfacial structure of GBs can be tailored to alter properties and performance.

One of the most pioneering studies for finding a route to mitigate intergranular fracture was done by Watanabe [4]. This study showed that it was possible to obtain both strong and ductile brass polycrystals with improved fracture resistance. This phenomenon was attributed to increasing the proportion of coincident site lattice (CSL) boundaries. CSL boundaries are characterized by specific misorientation values which allow the atoms to coincide at various points. Specifically, the relation between the number of lattice points in the unit cell of a CSL and the number of lattice points in the unit cell of the surrounding lattice is called its “Sigma” value (e.g. $\Sigma 5$, $\Sigma 11$, etc.) Figure 1.1 below shows this sigma relation for a $\Sigma 5$ symmetric tilt grain boundary. Here, two grains are tilted 18.44^{o} about their respective axes such that every fifth atom coincides with one another at the boundary.

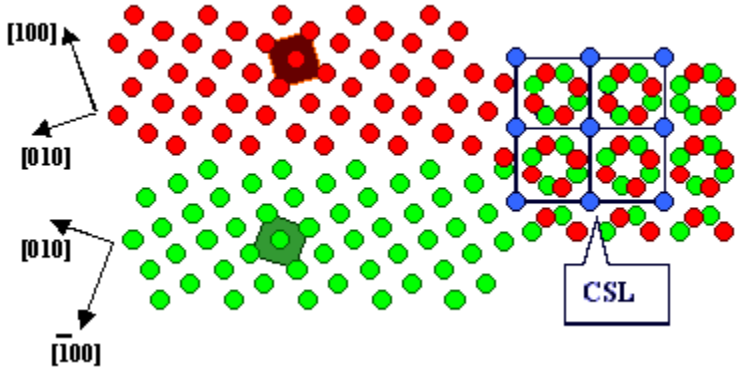

Figure 1.1: Snapshot of a Σ5 (100) GB with neighboring grains highlighted in red and green to show the characterization of a CSL boundary [5].

A few years after this study was done, another groundbreaking experiment was designed to improve the corrosion resistance of face centered cubic materials by altering the geometry of GBs [6]. This process eventually developed into the basis of grain boundary engineering (GBE).

One of the most notable successes of GBE was proven in the early 1990s in a study done by Lin et al. [7], which focused on increasing the corrosion resistance of nuclear steam generator tubing. They found that increasing the number of special boundaries (Σ≤29) resulted in

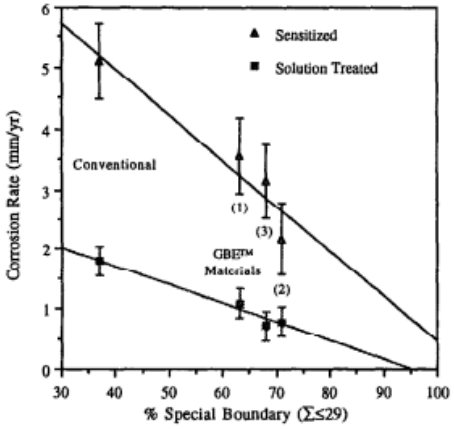

Figure 1.2: Corrosion rate measured as a function of % special boundary for the sensitized and solution treated samples through conventional and GBE processing routes [7].

a decrease in bulk intergranular corrosion susceptibility. Figure 1.2 clearly shows that the alloy process under the GBE method corrodes at a far slower rate than the conventional method of providing corrosion resistance. These findings were attributed to both the intrinsic corrosion resistance and resistance to solute precipitation exhibited by low-Σ GBs. Figure 1.3 shows the physical advantages of this processing route. Figure 1.3(a) exhibits heavy corrosion on the surface of the alloy, whereas (b) shows the increased resistance to corrosion and cracking because of the GB manipulation.

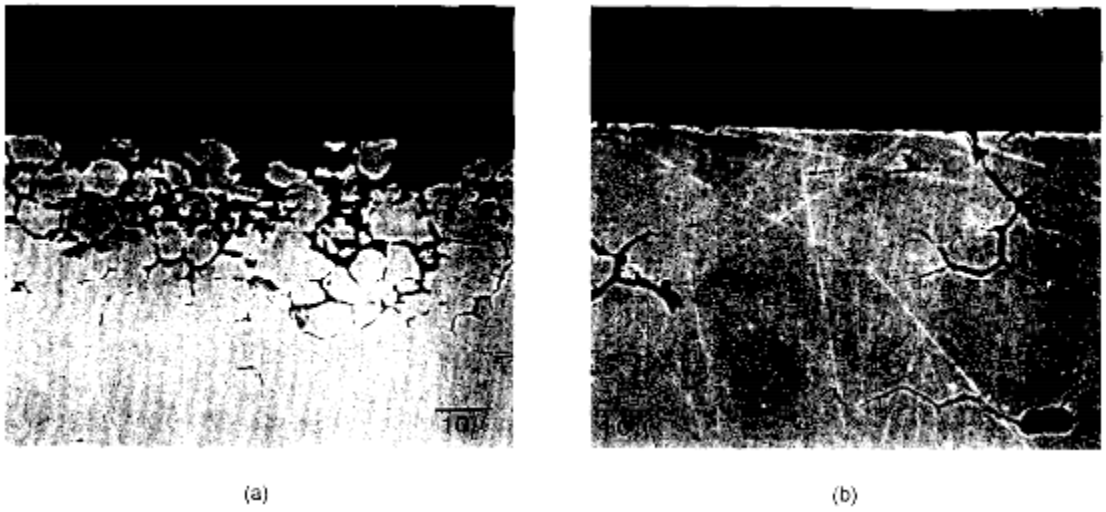

Figure 1.3: Cross-sectional SEM photographs [7] of (a) conventional and (b) GBE processed metal alloys following corrosion testing.

1.1.2 Segregation Engineering

Studies in more recent years have focused on the mechanisms of GBE. Specifically, a method called grain boundary segregation engineering (GBSE) focuses on understanding how solutes segregate to a GB to enhance the materials mechanical properties. A study by Herbig et al. [8] provided for a detailed physical analysis of GBSE in ferritic alloys. In Figure 1.4, we see that the segregating carbon directly contributes to the amorphous nature of the boundaries.

Moreover, low-angle GBs are shown to have a more direct effect on this behavior as we discussed earlier. GBE and its methods

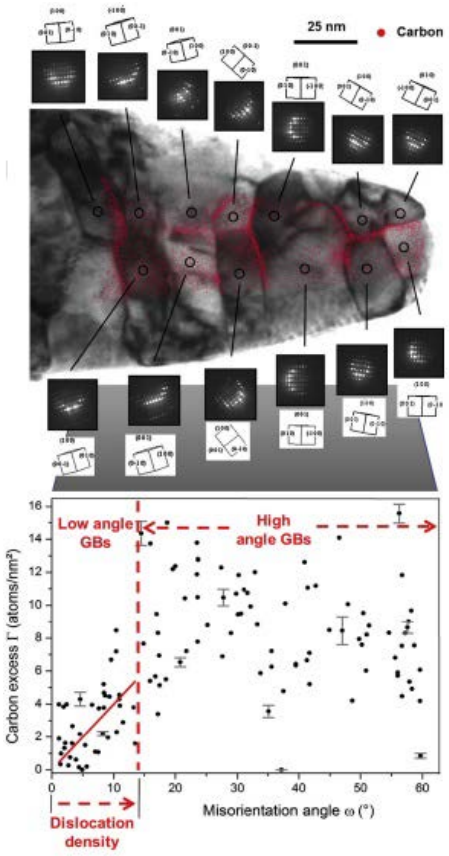

Figure 1.4: Quantifying GB segregation by using TEM (top) in the case of carbon segregating within ferrite. The lower plot shows the density of excess carbon atoms as a function of GB misorientation angle [8].

can be used to tailor the bulk mechanical strength and interfacial features of a polycrystalline sample.

1.2 Atomistic Simulations of Interfacial Phenomena

1.2.1 Molecular Dynamics Software

Atomistic modeling has played a key role in understanding interfacial interactions on very small timescales. Specifically, molecular dynamics (MD) software is used because of its adherence to classical mechanics laws. Quantum effects are not taken into account when

considering this method, which makes it a proper candidate for nano-scale behavior analysis. Perhaps one of the most readily available software packages for this vein of research is the open-source Large-scale Atomic/Molecular Massively Parallel Simulator (LAMMPS) program [9]. In LAMMPS, atomic positions within a coordinate system are established using various available interatomic potentials. These potentials give a physical representation of the atomic force interactions that are used to build the simulation [10]. Then, Newton's equation of motion (F = ma) is integrated from an initial timestep to the next timestep, which is typically 1 femtosecond, to update the relative displacements. Small scale interactions that occur rapidly can then be analyzed. Additionally, LAMMPS allows for the usage of commands called "fixes" which hold certain properties constant. Most notable are the NPT (constant number of atoms, pressure, and temperature), NVT (constant number of atoms, volume, and temperature), and NVE (constant number of atoms, volume, and total potential energy) fixes that control the thermodynamics of the simulation. Various outputs such as von Mises stress, atomic strain, and defect structure can be output with the thermodynamic data. Lastly, the boundary conditions placed on the simulation cell influence the mechanical and structural behavior of the cell. Periodic boundary conditions are applied to show that the simulation is representative of any three dimensional cross-section within the bulk of the material being studied. Free surfaces may be applied to allow for specific phase transitions or to alleviate internal stresses. This boundary condition is representative of a volume of material that exists right beneath the surface of the bulk phase.

1.2.2 OVITO

Another necessary tool that is used in atomistic simulations is visualization software. Once the MD script has finished, a series of thermodynamic data along with x,y, and z

coordinate positions are output. Simulation sizes can vary between 10,000 atoms to 1 billion atoms, so physically seeing how the system is reacting is crucial. A common open-source software package used is the Open Visualization Tool (OVITO) [11]. This tool assists the user in both visualizing atomic displacements and specific thermodynamic or mechanical quantities. One of the most common add-ons used in the literature are common neighbor analysis (CNA) [12], wherein atoms are identified by their associated structure types. Figure 1.5 shows a more detailed explanation of how this process works, specifically focusing on a study that investigated grain sliding.

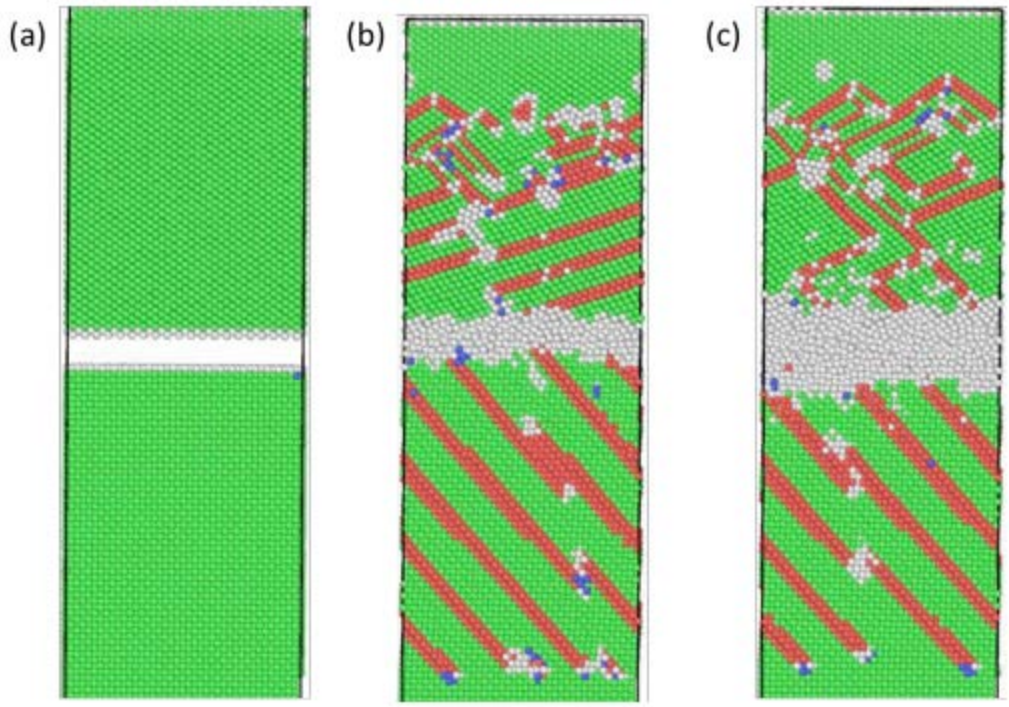

Figure 1.5: A sample simulation cell of a Ni-Ni bicrystal [13] at (a) 0 ps (b)12.5 ps and (c) 25 ps after grain sliding visualized by OVITO where green atoms are FCC, red are HCP, purple are BCC, and white are non-crystalline.

In Figure 1.5(a) two Ni grains are separated by a few atomic distances before they are drawn together as the sliding process begins. Shortly thereafter in (b), dislocations (in red) in the lower grain are clearly patterning throughout the cell as they impinge upon the GB. Lastly, at the end of the simulation in (c), we see that OVITO also captures the amorphous nature of the GB after undergoing dislocation absorption. This simplified case points to the necessity and power of efficient visualization software.

1.2.3 Analysis of Grain Boundary Structure in LAMMPS

Structural GB transitions have been investigated in more detail as simulation methods improve. One such MD study done by Frolov et al. [14] delves into understanding how the "split-kite" and "filled-kite" phases of a Σ5 (210) boundary reacts when coupled motion is involved. Figure 1.6 illustrates these phases more clearly. In Figure 1.6(a), it can

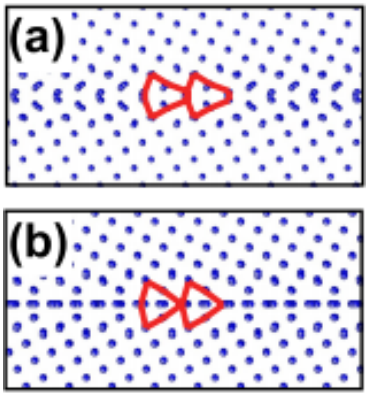

Figure 1.6: (a) Split-kite and (b) filled-kite phases of a Σ5 (210) GB after a 0K minimization [15].

easily be seen that there are no intermediary atoms filling this structure. However, in Figure 1.6(b), the "filled kite" structural phase contains atoms within the kites, indicative of a structural transition. These GB phase transitions can significantly affect the macroscopic properties of

materials, but the microstructural effects are still not well understood. Specifically, the effect of these transitions from coupled motion of GBs would elicit a clearer perspective of how the GBs operate. Figure 1.7 qualitatively and quantitatively examines this behavior. Figure 1.7(a) shows the migration path taken by the GBs after 30 ns of the shear-rate induced motion. A column of atoms was colored in red to indicate that the cell has obviously been sheared. Even though both of these cells had the same shear rate

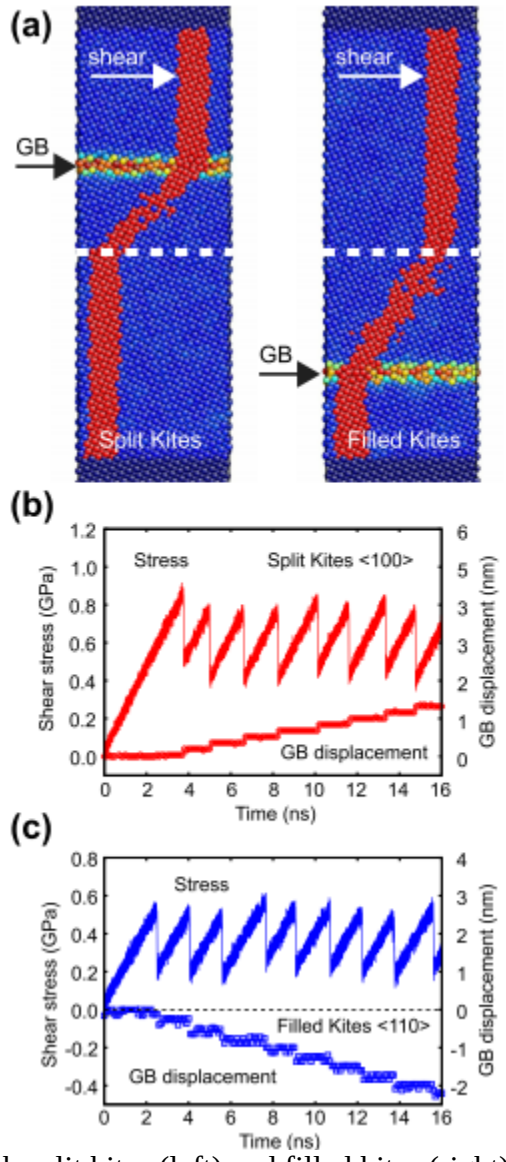

Figure 1.7: (a) Bicrystals with split kites (left) and filled kites (right) GB phases after 30 ns of coupled motion [14]. Initially vertical, the red atoms illustrate shear deformation. Shear stress and GB displacement measured as a function of time of (b) split kite and (c) filled kite phases.

imposed on them, it is important to note that the split kites GB (left) moved up whereas the filled kites GB (right) moved down. Figures 2(b) and 2(c) explain this behavior quantitatively. As the coupled motion begins in 2(b), we see a steady increase in GB displacement, but in 2(c) there is a gradual decline in the displacement. This behavior is attributed to the coupling factors described by equations (1.1) and (1.2) [14]:

$$\beta^{\langle 100 \rangle} = 2tan\left(\frac{\theta}{2}\right) \qquad (1.1)$$

$$\beta^{\langle 110 \rangle} = -2tan\left(\frac{\pi}{4} - \frac{\theta}{2}\right) \qquad (1.2)$$

which govern the coupling in the (100) and (110) modes, respectively. The split kite phase has a misorientation that closely identifies with (1.1), whereas the filled kite phase couples more closely to the (110) mode in (1.2). Since the only variable that was tuned during this study was the structural transition of the GB, it is evident that MD can be used to show how different structural phase transitions have a significant effect on kinetic properties of GBs.

1.3 Radiation tolerant interface design

1.3.1 Motivation

The expansive future of nuclear energy relies on a strong foundation of functional and safe design. Inside of a nuclear reactor, sub-atomic events called “collision cascades” are occurring at intensely high rates and volumes. High energy neutrons are colliding with the atoms of the bulk reactor material which leads to embrittlement and swelling [16].

Figure 1.8: Unirradiated steel (left) and steel that has been irradiated for a year (right) [17].

Figure 1.8 shows the consequences of collision cascades on a long timescale. The steel on the left in the figure has not been irradiated and thus retains its compact structure, whereas the irradiated steel on the right shows clear evidence of swelling. This behavior is linked to the catastrophic failure of most modern day reactors. Since GBs act as sinks for dislocations [18] and point defects such as voids or interstitials [19], designing the interfaces within a bulk material to be more radiation tolerant will certainly lead to better reactor output.

1.3.2 Defect Absorption at Grain Boundaries

Collision cascades take place in a matter of picoseconds, so MD is a reliable candidate for investigating how to tailor interfaces to make them more radiation resistant. This process is typically modeled by giving an atom within the bulk a large amount of kinetic energy and sending it through a GB [20]. A noteworthy finding first made by Sugio et al. [21] was that MD simulations of radiation damage near a GB consistently shows us that GBs absorb interstitials preferentially while leaving many vacancies in the bulk. This is the cause of the aforementioned reactor swelling. However, since the GB will be interstitial-rich, a process known as “interstitial emission” [20] may annihilate vacancies near the GB since interstitial migration is higher than the vacancy’s propensity to migrate. This fact influenced researchers to begin focusing on

tailoring not only the type of boundary, but also the mechanisms which influence GB sink efficiency.

Modern MD radiation damage studies have focused on tailoring the interfaces within a material. Understanding how to take advantage of point defect annihilation and minimizing bulk dislocation density are paramount to discovering efficient reactor materials. A study by Demkowicz et al. [22] showed that misfit dislocation networks formed at interfaces in Cu-Nb multilayers act as point defect recombination sites.

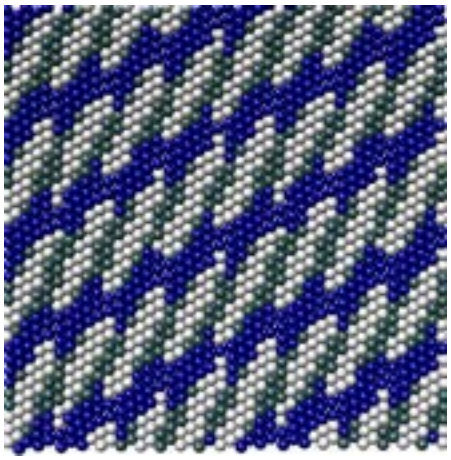

Figure 1.9: Cu atoms (white) and Nb atoms (blue) with misfit dislocations forming (green) at interfaces [22].

Figure 1.9 shows the effective simulation setup. Atoms were arranged in a Kurdjumov-Sachs orientation [23] where a Cu [111] plane neighbors an Nb [110] plane as this orientation has been thoroughly tested in the literature and allows for a controlled investigation of interfacial phenomena. Sample Cu atoms were then removed and inserted throughout this simulation cell to test its recovery mechanisms. Unlike in fcc Cu, removing a Cu atom in this setup does not lead to a vacancy, but instead a local defect reconstruction that finalized into the dislocations seen above. This study implies that the dislocations which arise from atom removal or insertion

enable these interfaces to reduce radiation damage. A similar study was done by Samaras et al. [24] which led to very different consequences. This MD study focused on collision cascades in nanocrystalline Ni, specifically measuring atomic displacement paths throughout the simulation. As mentioned earlier, GBs inherently have areas of free volume residing in their structure, and this fact is the basis of this paper's results. Samaras found that, during a collision cascade, affected atoms would move to a GB dislocation region and areas of free volume within the GB.

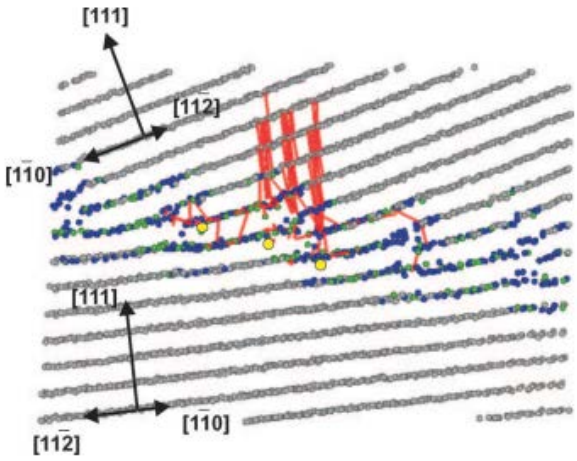

Figure 1.10: A selection of atoms during a collision cascade [24] (red) as they migrate towards the GB to dislocation regions and areas of free volume (yellow).

Figure 1.10 gives a visual depiction of the migration behavior. Atoms that have been impinged upon are given a large amount of kinetic energy and migrate towards the disordered GB. Therefore, this GB again preferentially absorbs self-interstitials and leaves vacancies remaining in the bulk. Coupling the studies in this section together we can conclude that (1) creating a material with a high volume fraction of interfaces increases its sink capacity and (2) interfaces with a higher degree of disorder and free volume act as efficient defect sinks.

1.4 Complexions

1.4.1 Definition and Identification

Researchers are currently in an ongoing process to identify nanoscale structural transitions and understand how they form. One idea gathering a lot of scientific support in recent years is the “grain boundary complexion”. According to Cantwell et al. [25], a complexion is “An interfacial material or strata that is in thermodynamic equilibrium with its abutting phases”. In other words, without the surrounding grains, this entity is not stable. Dillon et al. [26] originally began classifying these structure types using high resolution transmission electron microscopy (HR-TEM). They consolidated their data into six distinct complexion types as seen in Figure 1.11.

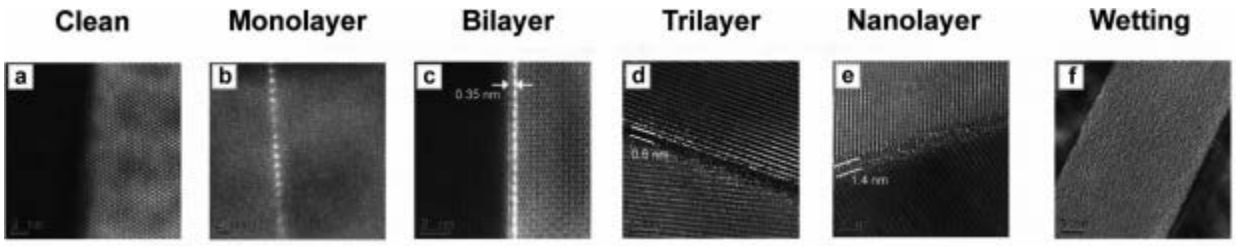

Figure 1.11: The six ascending complexion types (a)-(f) via HR-TEM [26]. The nomenclature has also been adapted to (a) clean (b) monolayer (c) bilayer (d) trilayer (e) nanolayer and (f) wetting [25].

Figure 1.11(a) starts with the clean grain boundary which is representative of a thin GB in a pure system. Figures 1.11(b), (c), and (d) are formed when dopant atoms for specific one, two, or three layer patterns aggregate within the GB. Figure 1.11(e) is a nanolayer film which is amorphous. Lastly, Figure 1.11(f) shows a wetting film, which is a fully disordered phase that forms at the boundary. These complexion types can be identified by thermodynamic measurements, such as grain boundary energy, and also their relative thicknesses.

1.4.2 Formation and Implementation

MD studies provide further insight into complexion formation by specifically focusing on lower-order complexion thermodynamics. Pan et al. [27] performed MD simulations investigating the likelihood of complexion formation given specific grain boundary character and energy. They found that the transition from ordered complexions to disordered intergranular films occurs either gradually or abruptly given a temperature-dependent value. Moreover, it was found that the ability to absorb dopant atoms at a GB, indicated by the relative amount of solute in excess, directly determines the propensity of a GB to form a complexion. Lastly, AIFs were shown to form at GBs with high solute excess. Conversely, GBs with low adsorption ability, such as ones found in systems where the solubility is negligible, do not favor formation of AIFs and transition abruptly. Frolov et al. [28] ran similar simulations focusing on lower-order complexion formation, but found free surfaces facilitate the process. Segregating Ag in their Cu-Ag system induces the formation of monolayers and bilayers depending on the global composition of the dopant. Both of these studies support that there is evidence of complexion formation in immiscible metal alloys under specific boundary and thermodynamic conditions.

Implementing GB complexions into existing metal alloys can have a profound effect on the mechanical properties of nanoscale samples [29]. Typically, there is a tradeoff between strength and ductility when considering bulk metal systems [30]. However, in a recent study by Khalajhedayati et al. [31], a unique combination of strength and ductility can be attained in Cu-Zr micropillars by tailoring the GBs of the system to form amorphous intergranular films (AIFs). These samples are initially annealed at high temperatures to “freeze” in the local disorder, much like a metallic glass, so that the segregating Zr remains at the boundary, thus influencing the formation of a complexion. In terms of simulations, this study also showed that

the AIF was able to absorb far more dislocations and accommodate more strain than a clean, ordered boundary.

1.4.3 Grain Boundary Complexion Diagrams

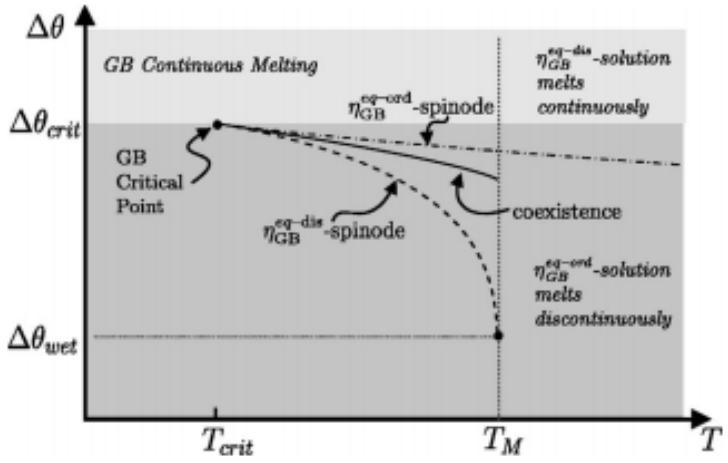

Figure 1.12: A GB-complexion diagram [32] where the solid line separates first-order GB transitions. The dotted lines mark the existence of metastable phases.

As the process of complexion formation is highly complex and thermodynamically-based, quantitative models have been sparse, but in-depth. Tang et al. [32] worked on developing GB complexion diagrams to better understand structural transitions. Figure 1.12 gives insight into this complexity. Misorientation angles for specific complexion types are plotted as a function of overall temperature. At low temperatures and misorientations, more ordered complexions are stable, whereas at high temperatures and misorientations, disordered complexions are more stable. The first order transition curve terminates at the GB critical point, wherein the transition becomes of a higher order. A similar study of grain boundary disordering in binary alloys by Luo et. al [33] led to the creation of thermodynamic diagrams that can detail

the projected thickness of an intergranular film. Figure 1.13 below shows Luo's addition to Tang's complexion diagram.

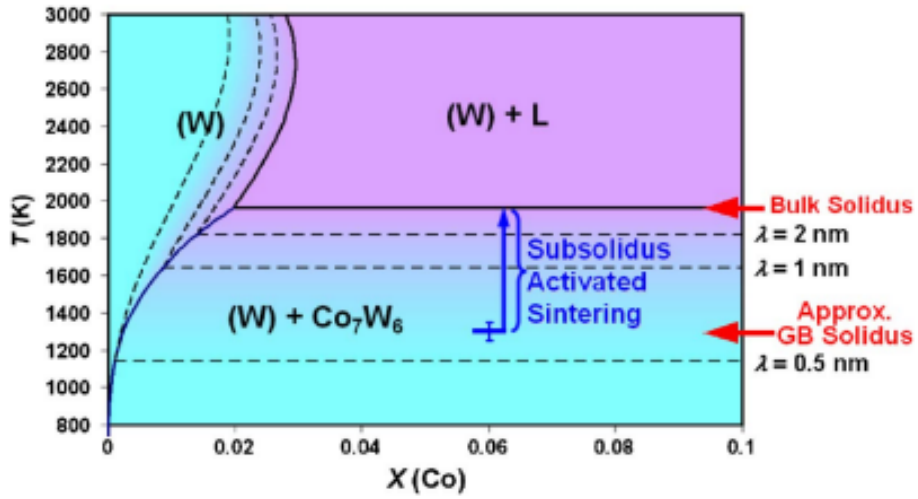

Figure 1.13: Lines of constant λ, which represent the thermodynamic tendency of stable intergranular films, are plotted on a GB phase diagram [33] concerning temperature as a function of global dopant concentration.

It is important to note in this figure that λ is constant in the two-phase region, whereas it decreases with decreasing dopant concentration in the single phase region. Moreover, subsolidus intergranular films are a sought after complexion type, so this graph implies that thermodynamics diagrams may exist for all the complexion types. Using these graphs, we can predict the likelihood of complexion formation in various binary alloy systems.

Chapter 2: Amorphous intergranular films act as ultra-efficient point defect sinks during collision cascades[1]

2.1 Introduction

The discovery of radiation-tolerant structural materials will play a vital role in the further development of nuclear energy technologies [16], as next-generation fission reactors and planned fusion technologies will require operation at higher radiation dosage rates. Inside a nuclear reactor, high-energy neutrons transfer kinetic energy to primary knock on atoms (PKAs), which then induce secondary collisions. These collision cascades create point defects within the material, with residual vacancies and interstitials eventually causing swelling and embrittlement that degrades mechanical behavior and leads to failure [35]. Historically, He ion bombardment has been used to replicate this process with lower PKA energies on the order of hundreds to thousands of electron volts. Experimental investigations of this type have shown that large He ion doses can cause defect planar clustering in Ni [36] and that a low angle grain boundary created by a network of edge dislocations can trap He in Mo at room temperature [37]. Recent research has suggested that the interfaces between crystallites (grain boundaries) can act as defect sink sites to help mitigate this problem [38], pointing to the promise of interface-dominated materials. For example, radiation-induced point defects are greatly reduced in layered Cu-V nanolaminates [39] and nanocrystalline Ni [40]. Similarly, nanostructured ferritic alloys [41] are possible candidates for radiation-resistant structures due to their larger interfacial volume fractions.

While prior work has shown that grain boundaries can increase the radiation tolerance of materials and nanostructuring has been pursued, the details of interfacial structure are also

[1] This chapter has been published as [34] J.E. Ludy, T.J. Rupert, Scripta Materialia, 110 (2016) 37-40.

important for sink efficiency. For example, Demkowicz et al. found that the misfit dislocation networks that form at heterointerfaces in Cu-Nb multilayers can act as templates for point defect recombination [22]. Similarly, Samaras et al. demonstrated that areas of free volume within a boundary can act as recombination sites for point defects [24]. If free volume is an important factor for sink efficiency, one can hypothesize that an amorphous intergranular film (AIF) would be a promising structural feature for radiation tolerance, since amorphous materials such as metallic glasses have been shown to have an excess amount of free volume [42]. Crystalline materials with stable amorphous interfaces can now be produced by deposition techniques such as co-sputtering, where amorphous layers are created by solid state amorphization [43], or segregation engineering [44], where segregating dopant atoms can induce amorphization by lowering the energy penalty of having a glassy interfacial phase [45]. In this study, we systematically compare collision cascade damage for a single crystal, an ordered grain boundary, and an amorphous intergranular film created by doping. Our results show that the AIF acts as an unbiased sink, absorbing both vacancies and interstitials, which is much more efficient than the ordered grain boundary.

2.2 Computational Methods

The process of PKA damage occurs on the nanometer length scale over a few picoseconds, making atomistic simulations an ideal tool for studying such an event. Atomistic simulations capture the initial point defect distribution after the cascade stops but miss long-range diffusion effects [46], yet have been used extensively to provide insight into damage mechanisms [20]. In this study, we use molecular dynamics (MD) run with the open-source Large-scale Atomic/Molecular Massively Parallel Simulator (LAMMPS) [9] code to simulate

PKA damage in Cu and Cu-Zr. Atomic interactions are described by a potential from Mendelev et al. [47] which recreates important properties of both the elemental systems, using Embedded Atom Method (EAM) formulations, and glassy Cu-Zr phases, using a Finnis-Sinclair formalism. The short range forces of this potential are represented by a molecular statics method [48] that calculates the force on each atom as:

$$F = F^{EAM} + \alpha F^{g} \qquad (2.21)$$

where F^{EAM} is the force calculated from the EAM data in the potential and αF^{g} is the force contribution from a tested hybrid algorithm. Together, these terms account for the overestimation of repulsion at small separation distances. An integration timestep of 1 fs is used for all simulations.

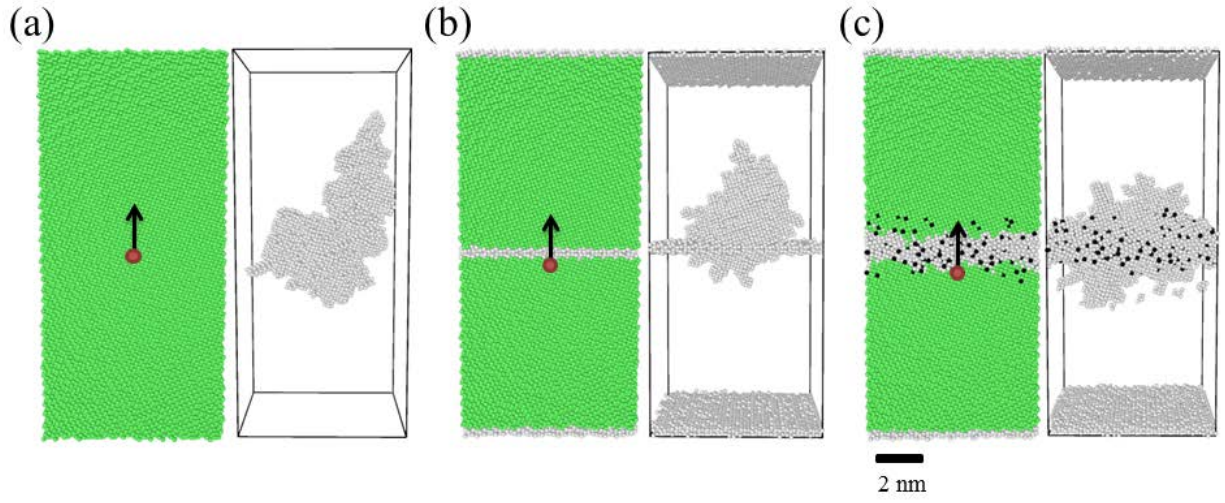

Figure 2.1: Collision cascade snapshots before (left) and during (right) cascade events of the (a) single crystal, (b) Σ5 (310), and (c) AIF structures with a PKA energy of 2000 eV. The PKA is colored red and directed upwards 0.5 nm away from each boundary. The green atoms are of the face centered cubic structure type and the white atoms are defects. The black atoms are Zr dopants.

The three test cases investigated here, shown in Figure 2.1, are a Cu single crystal, an undoped Σ5 (310) symmetric tilt grain boundary, and a 2.1 nm thick Cu-Zr amorphous intergranular film. In this figure, visualized by OVITO [11], crystalline Cu atoms are green, defect Cu atoms are white, and Zr atoms are black. These atom types were identified with adaptive common neighbor analysis [12] and all of our models consisted of ~108,000 atoms. The single crystal structure was used as a reference and had a [310] orientation with respect to the vertical axis of the simulation cell. A Σ5 (310) boundary was chosen to act as a model high-angle grain boundary, and was created by tilting both the top and bottom halves of a single crystal by 18.44° each about the [100] axis. To create the AIF, the Σ5 boundary structure was doped with 50 atomic % Zr in a 0.6 nm slice of material containing the boundary, heated locally to 1600 K to induce melting, and then cooled down to 300 K over 350 ps. This resulted in a 2.1 nm thick AIF with 15 atomic % Zr within the film.

Each simulation cell had periodic boundary conditions along all three axes to simulate a representative volume element of material. The models were equilibrated at 300 K and zero pressure under an isothermal-isobaric NPT (constant number of atoms, pressure, and temperature) ensemble for 10 ps. A PKA was then introduced at a distance of 0.5 nm from the interface with a velocity corresponding to 700, 1000, 1500, 2000, or 2500 eV of kinetic energy and directed upwards through the boundary, represented in Figure 2.1 as a red atom. The maximum PKA energy of 2500 eV was chosen because it is estimated to be the upper bound of what nanocomposites experience during He ion bombardment experiments [49]. The snapshots on the right in Figure 2.1 show the collision cascade of non-crystalline atoms at a PKA energy of 2000 eV when the ratio of non-crystalline to crystalline atoms is highest. The damage is

relatively dispersed throughout both the single crystal and ordered boundary, but is localized closer to the AIF. Each structure was simulated five times using different seed values for the initial temperature, giving a total of 75 simulations. Changing the seed value for temperature slightly alters the development of the cascade event, allowing for a statistical analysis of residual damage.

2.3 PKA Damage Process

For the next 52 ps, a microcanonical NVE (constant number of atoms, volume, and energy) ensemble was applied to the atoms in the cell interior where the collision cascade evolved. The boundary atoms were thermostatted at 300 K to simulate an infinitely large reservoir of room temperature material surrounding the cascade event, which forced the local temperature spike provided by the PKA to dissipate over time.

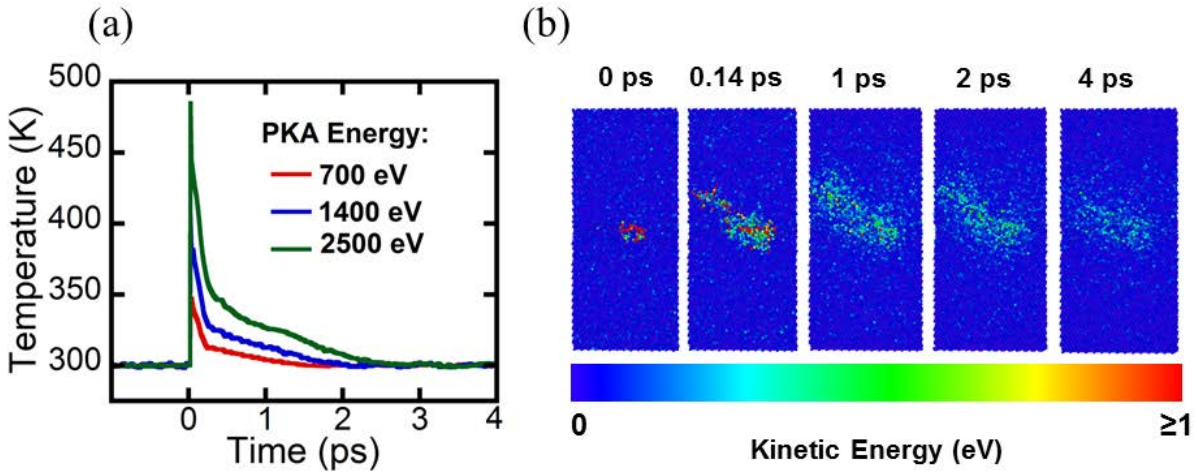

Figure 2.2: (a) The average temperature of the simulation cell in the AIF model during the 700, 1400, and 2500 eV PKA collision cascades. (b) The atomic kinetic energy distribution during a 2500 eV cascade. The cascades begin at 0 ps and the system cools down to 300 K over ~3 ps.

Figure 2.2(a) shows the system-average temperature of the simulation cell, demonstrating the thermal spike induced by three select PKA energies in the model with an AIF. Figure 2.2(b) illustrates the evolution of atomic kinetic energy for a 2500 eV PKA at an AIF. The collision cascade begins at 0 picoseconds and the elevated temperature cools down over ~3 ps. At the beginning of this event, the energy is concentrated around the cascade core, which accounts for the temperature peak. While most atoms have kinetic energies on the order of 0.01 eV, the few higher energy atoms visible at 0 ps and 0.14 ps contribute greatly to the development of a kinetically 'hot' core and the large increase in the average temperature of the simulation cell. Most point defect recombination (~98%) occurred during this early period, but a small percentage of the defects recombine during the remainder of the equilibration simulation. The temperature peak occurs right when the PKA is introduced and the magnitude is proportional to the PKA energy. As time progresses, the number of hot atoms decreases until average temperature returns to 300 K.

2.3.1 Voronoi Analysis

Defect atoms, first identified by adaptive common neighbor analysis, were further analyzed using the Voronoi tool incorporated into LAMMPS [50]. Each atom was first assigned a Voronoi volume where any point in space is closer to that atom than any other. At the end of the simulation, the number of atoms inside each initial Voronoi volume is then calculated. If a pair of atoms is occupying a single Voronoi volume, it is an interstitial.

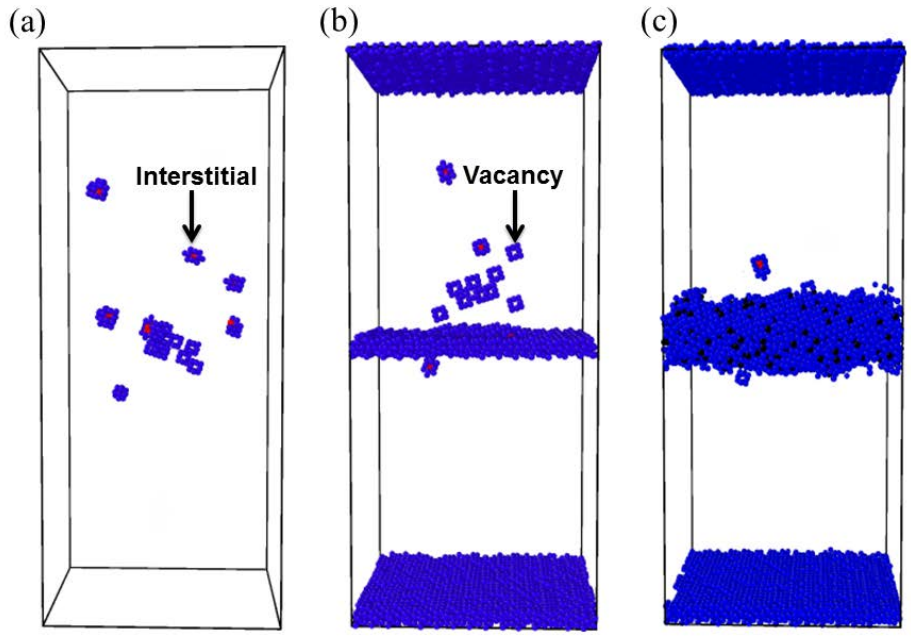

Figure 2.3: Post-equilibration snapshots of the (a) single crystal, (b) Σ5 (310) boundary, and (c) AlF models after a 2000 eV PKA. Voronoi volumes containing more than one atom are colored red (interstitials) and Voronoi volumes containing only one atom are colored blue. Zr atoms are colored black.

Figure 2.3 presents atomic snapshots of each model after the equilibration period has finished, with interstitials colored in red while defect atoms that retained one atom in their Voronoi volume are colored blue. In this figure, interstitials appear as a red atom surrounded by blue atoms, while vacancies appear as blue cells with the center atom missing. This tool does not explicitly find point defect types, but allows interstitials and vacancies to be manually counted by inspection according to the description above. For example, the Σ5 model shown in Figure 2.3(b) has ten vacancies and three interstitials left in the simulation cell. As seen in Figure 2.3(a), there are large numbers of residual interstitials and vacancies in the single crystal since direct recombination to eliminate Frenkel pairs is the only mechanism for defect annihilation. In the Σ5 model shown in Figure 2.3(b), there are fewer interstitials remaining in

the bulk because they have been absorbed by the boundary. However, similar to the observations of Bai and coworkers [20], many vacancies remain after equilibration. The AIF in Figure 2.3(c) absorbs both interstitials and vacancies more efficiently, leaving the model sparsely damaged. Moreover, the remaining defects are localized near the boundary, as opposed to the Σ5 case where defects are found further away from the interface.

2.3.2 Defect Quantification

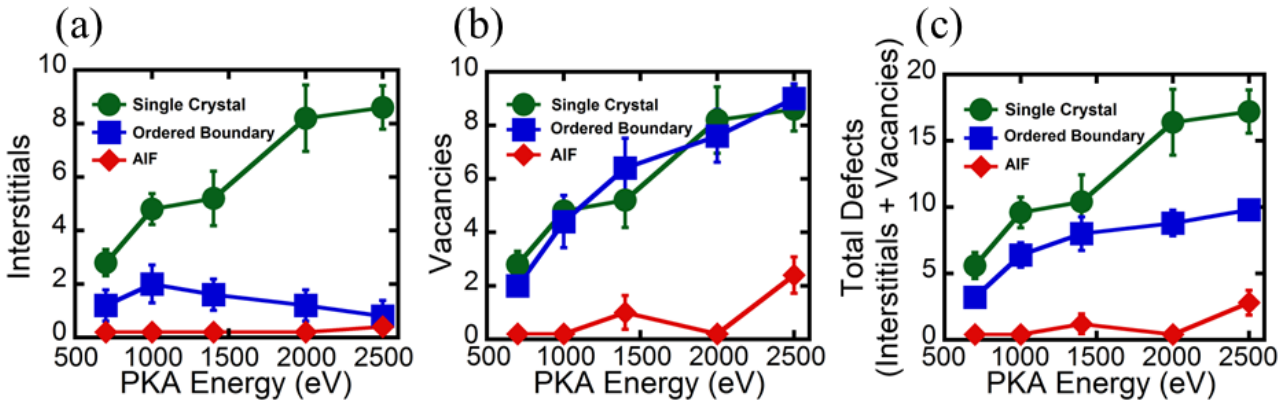

Figure 2.4: The number of residual (a) interstitials, (b) vacancies, and (c) total defects as a function of PKA energy. The Σ5 (310) boundary preferentially absorbs interstitials, but the AIF acts as a superior, unbiased sink.

Figure 2.4 plots the average number of residual point defects as a function of PKA energy for the three simulation groups. As a general trend, the number of defects increases with increasing PKA energy for all models. The increase in residual damage with PKA energy is simply explained by the fact that larger numbers of point defects are created at higher energies. The ordered grain boundary outperforms the single crystal model in absorption of interstitials, but is not a consistently better vacancy sink. Alternatively, the AIF acts as an unbiased defect sink over all energies.

2.4 Discussion

2.4.1 Effective Thickness

One reason for the improved sink efficiency of the AIF is its increased effective thickness. The cascade itself is far more contained within the 2.1 nm thick boundary when compared to the thin ordered grain boundary. Since the highest concentration of defects is produced near the center of the cascade [20], the defects are produced very close to where they can be absorbed. Caturla et al. used kinetic Monte Carlo simulations to show that large vacancy clusters form in the cascade core during an event [51]. This phenomenon can be taken advantage of with a thicker boundary, in terms of the kinetics of defect diffusion. Since the average mean free path for defect absorption will be shorter, more defects have the opportunity to be accommodated by a thicker boundary. While our current model does not account for recombination over longer time frames, a thicker boundary facilitates immediate defect absorption since damage is simply created closer to the sink.

2.4.2 Free Volume

The increased level of free volume in the AIF is likely another factor that leads to heightened point defect absorption. By again using an atomic Voronoi cell calculation, the volume associated with an average atom can be calculated for the single crystal, the ordered boundary, and the AIF. The average atomic volume associated with the single crystal can then be subtracted from the atomic volume within the ordered boundary and AIF to give a measure of free volume. While the ordered boundary only has a small amount of free volume when compared to the crystal (0.29 $Å^3$/atom), the AIF has ~4 times more free volume (1.16 $Å^3$/atom).

This corresponds to a 2 percent and 10 percent increase in average atomic volume for the ordered boundary and AIF, respectively. It is well known that amorphous materials such as metallic glasses retain an excess amount of free volume due to their atomic packing [52]. Structural modeling efforts by Miracle [53] suggest that this excess may result from densely packed solute-centered atomic clusters that make up the metallic glass. In this model, there is no orientational order amongst these clusters and face-sharing of neighboring clusters is preferred to minimize solvent volume. Recently, Ma suggested that the presence of geometrically unfavored polyhedra frozen in during rapid quenching may contribute additional free volume to the overall structure [54]. Faster quenching rates create more readily configurable polyhedra, which increases the overall free volume. Tschopp et al. used MD to study how grain boundary character influences point defect formation in ordered grain boundaries, finding that self-interstitial atoms have a larger energetic driving force for binding to general, high-angle grain boundaries than vacancies do [19]. Since this explains why ordered interfaces struggle to absorb vacancies, the absence of such behavior in AIFs suggests that the added free volume in an AIF creates an additional driving force for vacancy binding. The addition of Zr dopants to the AIF may also contribute to this phenomenon. In Kirchheim's theoretical study of formation energies, segregated solutes within a boundary or near a dislocation were found to lower local vacancy formation energies [55].

2.4.3 AIF Processing Routes

Recent advances in processing science have made crystalline materials with amorphous interfaces accessible in multiple material systems. Magnetron sputtering is a viable processing method for the creation of such materials. Wang et al. used this method to fabricate Cu-Zr

nanolaminates with alternating layers of crystalline Cu and amorphous Cu-Zr, created by solid state amorphization [43]. In this case, the thickness of the Cu-Zr amorphous layers could be tuned directly by controlling co-deposition times. However, this process is limited by low deposition rates and results in an anisotropic material, with the amorphous interfaces only being placed in the film growth direction. The formation of disordered interfacial complexions via segregation engineering [25] is a promising technique for introducing AIFs without such limitations. Shi and Luo developed the thermodynamic theory behind such disordered films, showing that doping can reduce the free energy penalty for the formation of AIFs and creating predictive grain boundary diagrams [14]. Tang et al. also developed a thermodynamic model incorporating interface energy and temperature [32], showing that disordered complexions are more stable at higher temperatures and that high-angle boundaries provide a more stable site for complexions than low-angle grain boundaries. An implication of these models is that AIFs may be introduced into a random polycrystalline material if segregating dopants are added and high temperature grain boundary structures are quenched into the microstructure, with thickness perhaps controlled by tuning dopant concentration and temperature.

2.5 Conclusions

Our molecular dynamics simulations suggest that amorphous intergranular films act as efficient point defect sinks when compared to general, high-angle grain boundaries. Increasing the effective interfacial thickness allows for shorter point defect migration distances, while the excess free volume present in an AIF dramatically increases the absorption of vacancies. The extremely rapid healing of cascade damage at an AIF should be beneficial for nuclear reactor materials which must survive high dosage rates. Incorporating AIFs into nanostructured

materials would place these damage-tolerant interfaces regularly throughout the material, offering a promising route for unprecedented resistance to radiation damage

Chapter 3: Formation of structurally ordered and disordered intergranular films in immiscible metal alloys

3.1 Introduction

In recent years, the idea of grain boundary complexions have garnered a lot of attention and research support due to their complicated structure and potential for usability across a myriad of applications [29]. Complexions are interfacial materials that are in thermodynamic equilibrium with their abutting phases that have a stable, finite thickness [25]. Ordinary grain boundaries can be analyzed using equilibrium thermodynamics [56] and may have structural transitions similar to that of their bulk counterparts, but complexions do not satisfy this Gibbs definition of a phase because they are inhomogeneous across compositions and structure [29]. Complexion transitions have been shown to be responsible for diverse behavior such as abnormal grain growth [26], solid-state activated sintering [57], and increased ductility in a Cu-Zr system [31]. Intergranular films are higher type Dillon-Harmer complexions that can be structurally and chemically ordered or disordered. Dopants in monolayer, bilayer, or trilayer complexions form specific segregation patterns at the grain boundary, while amorphous intergranular films (AIFs) and wetting phases are completely disordered structurally and chemically [26]. Most notably, pre-melting [58]-[59] and amorphous film formation [60]-[61] have been focused on, whereas lower type complexion studies comprise a subset of the literature.

Since dopant segregation and complexion formation are nanoscale processes, atomistic simulations are an ideal tool for studying intergranular film and sub-intergranular film complexions. Molecular dynamics (MD) has been used to study the pre-melting behavior of intergranular films in pure and Ag-doped Cu [62] as well as the kinetics of intergranular film formation [63]. Frolov et al. have used MD to discover two different grain boundary phases that

exist when using the Σ5 (310) symmetric tilt grain boundary in a Cu-Ag system [28]. This gives rise to phase transformations as a consequence of changing chemical composition while the temperature is fixed. Frolov et al. also went on to find that adding a free surface to the system would enable a transformation in the same Σ5 (310) grain boundary [15]. Recently, Pan and Rupert used atomistic simulations to study disordering transitions in Cu-Zr [27], finding that different ordered complexions first form , depending on the boundary's starting structure, and that a transition to a structurally disordered state occurs at high boundary concentrations of Zr. They also found that a boundary's tendency to undergo the disordering transition more directly linked to the relative solute excess than the starting grain boundary energy. Purely thermodynamic models for complexion formation have been developed as well. Luo and Shi performed a study on disordering in binary alloys showing that equilibrium complexion diagrams can be created to see the effects of temperature and global dopant concentration on the formation of specific complexion types [33]. However, studies investigating intergranular film formation in binary alloys with different enthalpies of mixing have not been well established. Systems such as Cu-Nb that are immiscible with negligible solubility [64] and contain few intermetallics may provide further insight into how ordered and disordered films form. Since these materials do not form intermediate phases, adjustable cooling rates may not maintain the disorder enabled at higher temperatures as it is equilibrated [65]. Moreover, these kinds of systems are needed to bridge the gap between current knowledge of binary alloy disordering and intergranular film formation.

In this paper, we use MD to analyze the behavior of Σ5 (013) and Σ11 (113) boundaries in Cu-Zr and Cu-Nb systems to further develop the notion of how segregating dopants affect intergranular film formation. The Cu-Zr system consistently forms amorphous films whereas the

Cu-Nb system forms both ordered and disordered films. At higher temperatures, a disordered transition is seen for Cu-Nb in the Σ5 (310) boundary at low dopant percentages, but remains ordered otherwise. A free surface is then applied to the 600 K Σ11 (113) boundary samples to give insight into how the behaviors are implemented across different boundary conditions.

3.2 Computational Methods

In this study, a hybrid simulation technique comprised of Monte Carlo modeling of chemical distribution and MD simulation of local structural relaxations is run using the open-source Large-scale Atomic/Molecular Massively Parallel Simulator (LAMMPS) code [9]. Atomic interactions for Cu-Zr are described by a potential from Mendelev et al. [47] which recreates important properties of both the elemental systems (using Embedded Atom Method (EAM) formulations) and glassy Cu-Zr phases (using a Finnis-Sinclair formalism). An EAM potential created by Liang et al. [66] is used for Cu-Nb interactions because of its adherence to the topological features of the experimental equilibrium phase diagram in both solid and liquid states. This potential is also fitted to the elements respective enthalpies of mixing. Both Σ11 (113) and Σ5 (013) tilt grain boundaries were investigated at 600 K and 1200 K to understand different complexion behavior at low and pre-melting temperatures. These two boundaries were chosen because they differ significantly in grain boundary energy (Σ11 (113) = 0.022 eV $Å^{-2}$ and Σ5 (013) = 0.062 eV $Å^{-2}$) [27] and potential dopant sites. Each simulation cell consisted of ~165,000 atoms arranged in a rectangular prism (22 nm x 22 nm x 4.45 nm) with two interfaces in each system. Periodic boundary conditions were used for the majority of the simulations, although the effect of free surfaces will be discussed later in the paper. The simulation cell was first run through a conjugate-gradient minimization and then equilibrated at the appropriate

temperature under zero pressure with an isothermal-isobaric ensemble (constant number of atoms, pressure, and temperature) for 5 ps. The simulation was then run using the variance-constrained semi-grand canonical (VC-SGC) ensemble [67]. Every 100 MD steps, a Monte Carlo step is performed to adjust the chemical potential and thus global dopant concentration of the cell until its total potential energy converged below a given variation tolerance of .0014 keV. MD steps were typically run for 3 to 5 ns depending on the target concentration that needed to be reached. Under the VC-SGC ensemble, a suitable choice of chemical potential affects the real-time run rate of the simulation and the global dopant concentration [62]. To monitor this variable, we used a self-evaluating script that adjusted the chemical potential after every 1000 steps to ensure the maximum global concentration was reached. Our initial estimations for the chemical potential difference were 3.5 and 3.7 eV for the Cu-Zr and Cu-Nb samples, respectively. After the total potential energy reached a minimum value, the simulation was placed under another conjugate-gradient minimization to remove thermal noise. All atomistic configurations are visualized using OVITO [11] and the structure types were identified with adaptive common neighbor analysis (CNA) [12]. Atoms were also colored by atom type to give a clearer view of how the dopants segregated to the interfaces.

3.3 Results and Discussion

3.3.1 Qualitative Structural Transition Results

At low dopant compositions, there is a clear difference between the segregation behavior of Nb and Zr in our system. As seen in another study [27], nanoscale amorphous intergranular films (AIFs) form in a Σ11 (113) boundary far beneath the melting temperature of Zr. The left

images of Figure 3.1 (a)-(c) shows the evolution of these complexions as the dopant composition is increased.

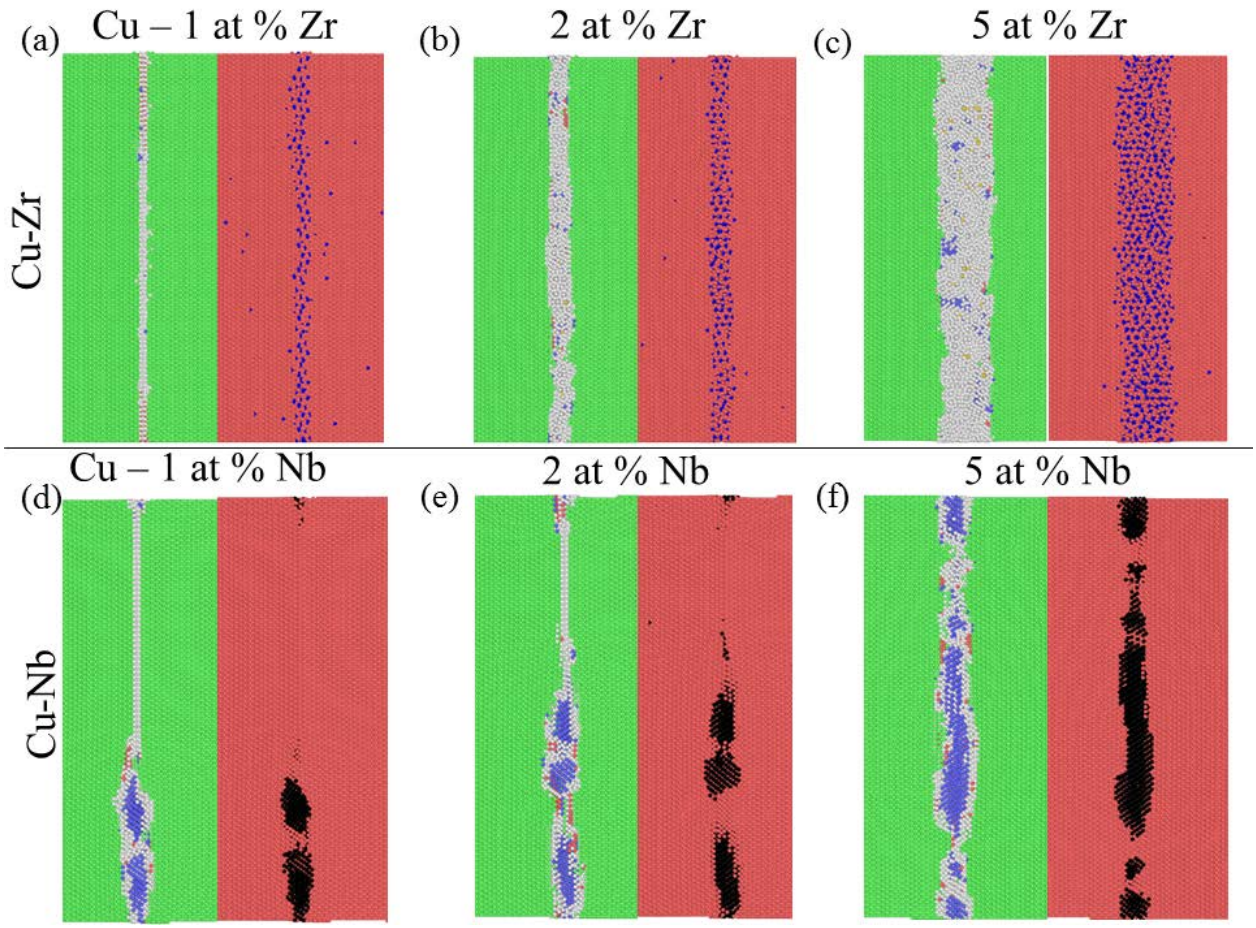

Fig. 3.1. Snapshots of singular Σ11 (113) grain boundaries doped at 600 K in the (a)-(c) Cu-Zr and (d)-(f) Cu-Nb systems with periodic boundary conditions. The left picture in each pair represents the structure of the atoms where white atoms are non-crystalline, green atoms are FCC, red atoms are HCP, purple atoms are BCC, and icosahedral atoms are yellow. The right picture shows the chemistry of the boundary where peach atoms are Cu, blue atoms are Zr, and black atoms are Nb.

Multiple structure types are easily identified in this figure as compositions are increased which is evidence of increasing disorder. Similarly, focusing on the chemistry of the sample in the right half of (a)-(c), we see the Zr form into a fully disordered film. Figure 3.1 (d)-(f) shows Nb

exhibiting a much different behavior when it is the primary dopant. As seen in the left half of the figure, atoms in the boundary aggregate together to form a crystalline BCC phase since the solubility of Nb in Cu is almost negligible, especially at temperatures beneath the melting point of Nb [68]. Coupled with the right half of Figure 3.1 (d)-(f), we can see that all of the Nb atoms form these phases. As dopant composition is increased, Nb prefers to segregate to areas in the boundary that will cohesively lengthen the ordered Nb phase. The Nb dopants form continuous phases within the boundary until a boundary solubility limit is reached and then they partition into ordered phases separated by smaller non-crystalline boundaries within the main boundary.

3.3.2 Quantitative Structural Transition Results

Figure 3.2 represents a quantitative perspective of the phenomena described above. Grain boundary thickness is measured as a function of global dopant composition in Figure 3.2(a), which gives insight into the process of complexion categorization. The Cu-Zr system smoothly transitions into an AIF after one percent of Zr is added.

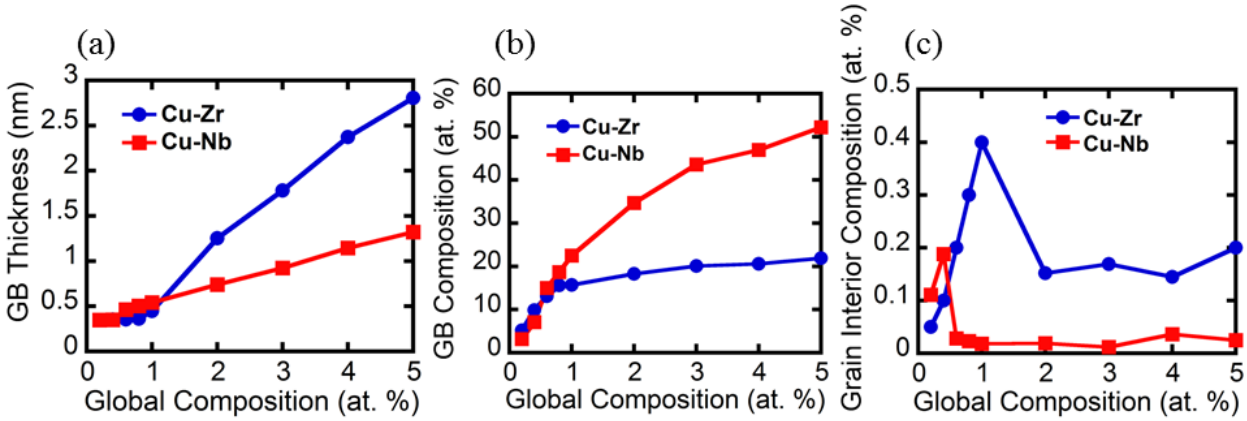

Fig. 3.2. (a) Grain boundary thickness, (b) grain boundary composition, and (c) grain interior composition as a function of global composition for the Σ11 (113) samples with periodic boundary conditions doped at 600 K.

After this, the boundary thickness increases rather quickly and these thicknesses fall within the range of nanoscale AIFs [27]. However, the Cu-Nb transition to an ordered phase is rather abrupt. At ~0.6% global composition, the Nb dopants aggregate together in a boundary resulting in this sharp increase of thickness. After this, the thickness increases almost exactly linearly. As more Nb is added, it segregates directly to the phases in the boundary. Figure 3.2(b) shows how direct this behavior is. After the ordered Nb transition, grain boundary compositions quickly climb to more than fifty percent, whereas the Zr composition remains relatively constant. Figure 3.2(c) shows a similar result concerning the grain interior composition. In the case of Zr, a small, constant amount of dopant remains outside of the grain boundary after an amorphous transition. Conversely, after the crystalline Nb transition, virtually 0% of the dopant remains in the grain interior. Nb has a greater propensity to segregate and form ordered phases as opposed to Zr.

3.3.3 Effect of Varying Grain Boundary Character

Grain boundary character plays an important role in determining the likelihood of forming a disordered intergranular film. In Figure 3.3, we have illustrated what happens when the character of the boundary is changed, coupled with an increase in temperature. This increase in temperature was made to facilitate grain boundary segregation since the system will be close to the melting point of the dopants used, thus leading to enhanced migration. At low dopant compositions, the Nb-doped Σ11 (113) boundary in Figure 3.3(a) remains essentially untouched. Structurally speaking, the boundary is not perturbed. Figure 3.3(b) shows how Nb is intermittently dispersed throughout the cell as much of the dopant remains in the grain interior. Similar to the behavior seen in our 600 K samples, Figure 3.3(c) shows how the boundary

immediately forms an ordered film at 6 at. % composition. Another important result is that this boundary can contain more Nb before forming a crystalline phase. In our 600 K samples, the Σ11 (113) boundary had its crystalline transition before one percent Nb, whereas the 1200 K Σ11 (113) boundary can sustain up to 3 percent Nb without transitioning. The Σ5 (013) boundary in Figure 3.3 (d)-(f) exhibits very different behavior.

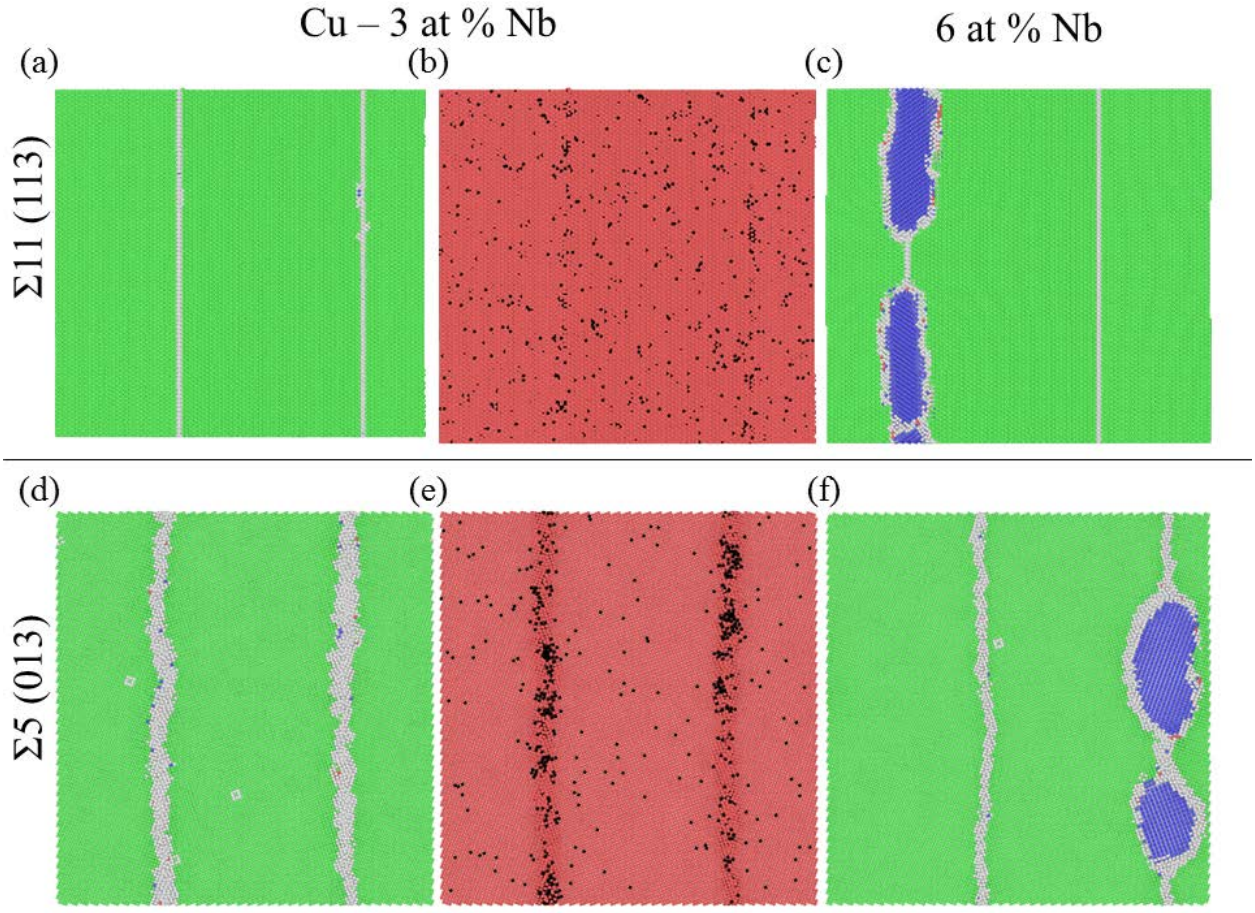

Fig. 3.3. Structural analysis of the Nb-doped [(a) and (c)] Σ11 (113) boundary and [(d) and (f)] Σ5 (013) boundary at 1200 K with periodic boundary conditions. White atoms are non-crystalline, green atoms are FCC, red atoms are HCP, purple atoms are BCC, and yellow atoms are icosahedral. (b) and (e) are the chemistry analysis of the Σ11 (113) boundary and Σ5 (013) boundary, respectively, where peach atoms are Cu and black atoms are Nb.

At low dopant composition in Figure 3.3(d), the boundary thickens and is disordered. In Figure 3(e), we can see how Nb has segregated to the boundary, but not in a fully disordered fashion.

Some of the atoms have aggregated together, but not with such propensity as to form their own ordered phase. However, as the composition is increased in Figure 3.3(f), we see that the Nb forms a crystalline phase as seen in the Σ11 (113) boundary. Simply altering the grain boundary structure led to far different behavior at low dopant compositions.

3.3.4 Effect of Free Surface on Structural Transitions

Lastly, we investigated the effect of free surfaces on our system. Figure 4 shows the dopant segregation behavior during select compositions of the dopant's initial formation, intermediate progression, and final covering. In Figure 3.4(a), The Zr dopants initially aggregate right above the triple junctions.

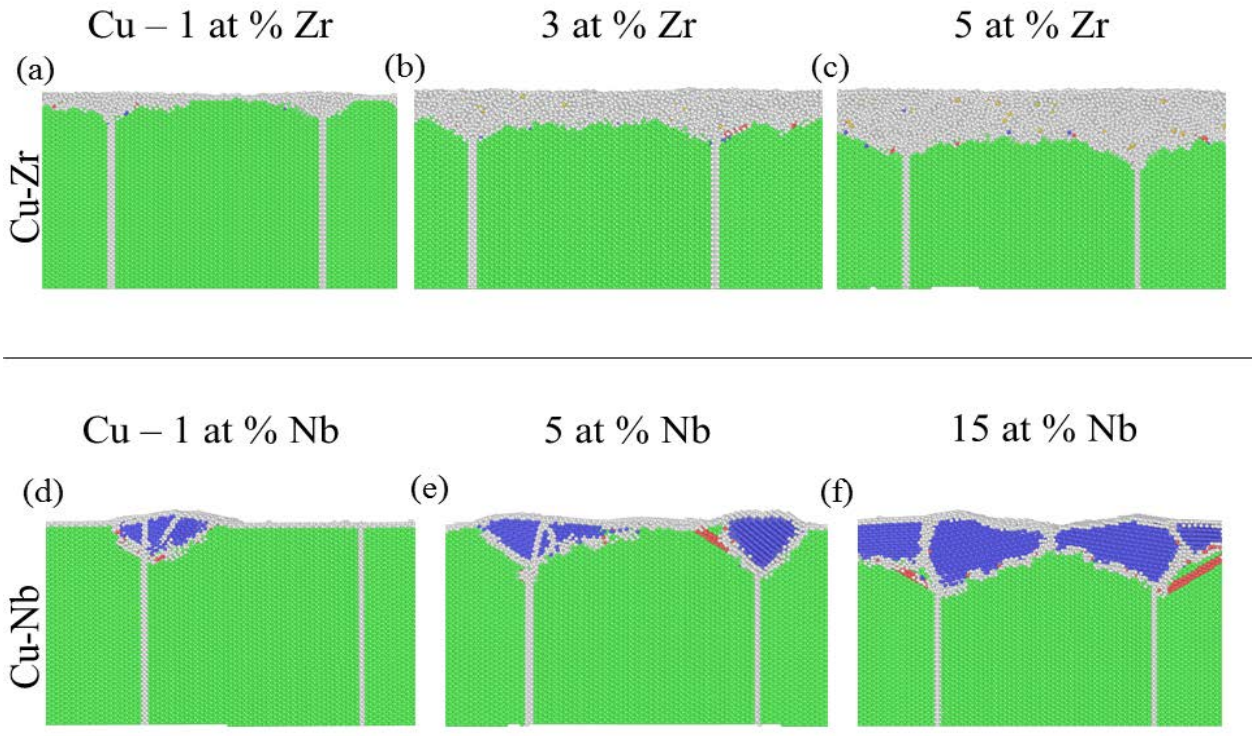

Fig. 3.4. The structure types of the top halves of the Σ11 (113) samples at 600 K with an upper and lower free-surface doped with (a)-(c) Zr and (d)-(f) Nb. White atoms are non-crystalline, green atoms are FCC, red atoms are HCP, purple atoms are BCC, and yellow atoms are icosahedral.

This may be a consequence of the surface-to-grain-boundary energy ratio being greater than $\sqrt{3}$, thus making the triple junction line unstable [69]. Segregating dopants are known to potentially lower both of these values [70], thus making the system more stable. As the composition is increased in Figure 3.4(b), the Zr dopants fully disorder the free surface leaving the grain boundaries intact. At the highest composition in (c), the free surface begins to envelope the boundary, forming a wetting phase. The Zr has segregated mostly to the free surfaces, causing the overall disorder. As for the Nb dopants, there is a more well-defined progression throughout the free surface. The most favorable position within our system for the Nb to initially segregate to is the triple junction, as this may be the most energetically favorable position to begin as shown in Figure 3.4(d). After this, the Nb disperses throughout the rest of the free surface and eventually within the grain boundaries themselves in Figure 3.4(e). An important behavior to note is again the ordered nature of the phases formed by Nb. The Nb dopants form singular BCC phases with partitions in between them at the higher compositions as seen in earlier simulations. Coupled with this behavior, stacking faults (HCP structure type) and other defects start to arise due to the interior stress build up from this segregation. As discussed before, a very small minority of Nb dopants remain within the boundaries as the phase transitions are taking place.

3.4 Conclusions

In this paper, we used a combination of Monte Carlo/MD simulations to assess the role of segregating dopants in the Cu-Zr and Cu-Nb systems with respect to ordered and disordered film formation by varying grain boundary character and temperature. Zr dopants form disordered amorphous films under all periodic boundary conditions. Alternatively, we found that immiscible dopants with almost negligible solubility in Cu such as Nb form distinct, crystalline

phases within grain boundaries at temperatures far beneath its melting temperature in Σ11 (113) boundaries. Near Cu pre-melting temperatures, the Σ11 (113) boundary can contain more Nb before structurally transitioning to ordered phases. However, in a Σ5 (013) boundary at low Nb dopant compositions, there is a high degree of disorder within the boundary. Although this behavior greatly contrasts with the Σ11 (113) boundary, the Σ5 (013) boundary encounters a crystalline transition at higher global compositions as well. Adding a free surface to these systems allows both of our dopants to segregate outside of the boundary to a more energetically favorable state. The Zr dopants form a wetting film at the surfaces that slowly envelopes the Σ11 (113) boundary with increasing composition, whereas the Nb dopants start distinctly at the triple junctions and then coalesce to form a crystalline phase. While both of these dopants have similar properties in a Cu system, it is evident that efficient glass-forming binary systems are more likely to form disordered complexions while extremely low solubility systems with differing enthalpies of mixing will form crystalline phases within the grain boundary given specific boundary conditions and grain boundary character.

Chapter 4: Summary and Conclusions

4.1 Summary

Two comprehensive MD studies were performed to give insight into the intricacies of creating radiation resistant materials and understanding structural transitions in binary alloys. Specifically, simulations are used to explore the effect of interfacial structure on residual radiation damage. An ordered grain boundary is compared to a disordered amorphous intergranular film, to investigate how interface thickness and free volume impacts point defect recombination. Collision cascades are simulated and residual point defect populations are analyzed as a function of boundary type and primary knock on atom energy. Secondly, hybrid Monte Carlo/molecular dynamics simulations are used to study segregation-induced intergranular film formation in Cu-Zr and Cu-Nb alloys. While Cu-Zr alloys form structurally disordered or amorphous films, second phases precipitate at the interfaces of Cu-Nb. Finally, the effect of free surfaces on dopant segregation and complexion formation is investigated for both alloys.

4.2 Conclusions

Our molecular dynamics simulations suggest that amorphous intergranular films act as efficient point defect sinks when compared to general, high-angle grain boundaries. Increasing the effective interfacial thickness allows for shorter point defect migration distances, while the excess free volume present in an AIF dramatically increases the absorption of vacancies. The extremely rapid healing of cascade damage at an AIF should be beneficial for nuclear reactor materials which must survive high dosage rates. Incorporating AIFs into nanostructured materials would place these damage-tolerant interfaces regularly throughout the material,

offering a promising route for unprecedented resistance to radiation damage. Our Monte-Carlo/MD models show that structural GB transitions rely heavily on grain boundary character and the material alloy system that is being tested. Cu-Zr GBs form nanoscale films after a specific dopant tolerance composition, whereas Cu-Nb systems form complete second phases at the GB. However, at higher temperatures, the Σ5 (013) exhibits behavior that is dependent on grain boundary character. While the ordered complexion is retained at high temperature for the Σ11 (113), a disordering transition is observed for high energy Σ5 (013) boundaries at low dopant concentrations. The ordered film structure reemerges as dopant concentration is increased.

Chapter 5: Future Work

Many avenues of experimentation and modeling can be investigated from the work of this thesis. In terms of MD, the radiation tolerant interface findings can provide a basis for a much more developed study that uses a system of millions of atoms and a longer timescale. Different complexion types or varying GB character could also be modeled after our bicrystal setup to test their respective sink efficiencies. Experimentally, AIFs can be incorporated into nanoscale systems to physically test their sink efficiencies. AIFs are known to dramatically increase the ductility of a Cu-Zr nanoscale system [31], so it would be worth attempting such implementation into materials that can be tested under irradiated environments.

The complexion interface thermodynamics project can be extended in a similar manner. More GB types can be modeled to better understand mono- and bilayer complexion type formation. In addition to changing the boundary type, the alloy system can be amended to other immiscible types such as Cu-Ta to test for the immediate or gradual structural transition at the GB. Both the Cu-Zr and Cu-Nb systems can be fabricated by sputtering methods as well to test their viability as structural components. Different boundary types can be analyzed via TEM to single out specific GB characteristics and identify suitable structures to be mechanically tested.

Lastly, these different complexion types can be tested under extreme environments for the purpose of assessing their stability. The amount of literature concerning complexion formation and thermodynamics is steadily growing, but physical tests of their viability under non-ideal conditions (e.g. very high or very low temperatures, highly pressurized vessels, etc.) are the next frontier for developing a fully interconnected understanding of how complexions behave.

References

[1] P.E.J. Flewitt, R.K. Wild, Grain Boundaries: Their Microstructure and Chemistry, by PEJ Flewitt, RK Wild, pp. 338. ISBN 0-471-97951-1. Wiley-VCH, April 2001., (2001) 338.

[2] J.E. Flinn, D.P. Field, G.E. Korth, T.M. Lillo, J. Macheret, Acta Materialia, 49 (2001) 2065-2074.

[3] H.B. Aaron, G.F. Bolling, Surface Science, 31 (1972) 27-49.

[4] T. Watanabe, Res Mechanica, 11 (1984) 47-84.

[5] H. Foll, in, 2005. <
http://www.tf.unikiel.de/matwis/amat/def_en/kap_7/backbone/r7_1_2.html
>

[6] G. Palumbo, P.J. King, K.T. Aust, U. Erb, P.C. Lichtenberger, Scripta Metallurgica et Materialia, 25 (1991) 1775-1780.

[7] P. Lin, G. Palumbo, U. Erb, K.T. Aust, Scripta Metallurgica et Materialia, 33 (1995) 1387-1392.

[8] M. Herbig, D. Raabe, Y.J. Li, P. Choi, S. Zaefferer, S. Goto, Physical Review Letters, 112 (2014) 126103.

[9] S. Plimpton, Journal of Computational Physics, 117 (1995) 1-19.

[10] F. Ercolessi, J.B. Adams, EPL (Europhysics Letters), 26 (1994) 583.

[11] A. Stukowski, Modelling and Simulation in Materials Science and Engineering, 18 (2010) 015012.

[12] A. Stukowski, Modelling and Simulation in Materials Science and Engineering, 20 (2012) 045021.

[13] K. Chen, M. Zeng, L.-B. Wang, Q. Wang, in: ICHMT Digital Library Online, Begel House Inc., 2015.

[14] T. Frolov, Applied Physics Letters, 104 (2014) 211905.

[15] T. Frolov, D.L. Olmsted, M. Asta, Y. Mishin, Nature Communications, 4 (2013) 1899.

[16] S.J. Zinkle, G. Was, Acta Materialia, 61 (2013) 735-758.

[17] University of Washington, Physics Dept, (2009). <
http://cmcsn.phys.washington.edu/book/export/html/507>

[18] M.W. Grabski, R. Korski, Philosophical Magazine, 22 (1970) 707-715.

[19] M.A. Tschopp, K. Solanki, F. Gao, X. Sun, M.A. Khaleel, M. Horstemeyer, Physical Review B, 85 (2012) 064108.

[20] X.-M. Bai, A.F. Voter, R.G. Hoagland, M. Nastasi, B.P. Uberuaga, Science, 327 (2010) 1631-1634.

[21] K. Sugio, Y. Shimomura, Tomas D.de l. Rubia, Journal of the Physical Society of Japan, 67 (1998) 882-889.

[22] M. Demkowicz, R. Hoagland, J. Hirth, Physical Review Letters, 100 (2008) 136102.

[23] P.M. Anderson, J.F. Bingert, A. Misra, J.P. Hirth, Acta Materialia, 51 (2003) 6059-6075.

[24] M. Samaras, P. Derlet, H. Van Swygenhoven†, M. Victoria, Philosophical Magazine, 83 (2003) 3599-3607.

[25] P.R. Cantwell, M. Tang, S.J. Dillon, J. Luo, G.S. Rohrer, M.P. Harmer, Acta Materialia, 62 (2014) 1-48.

[26] S.J. Dillon, M. Tang, W.C. Carter, M.P. Harmer, Acta Materialia, 55 (2007) 6208-6218.

[27] Z. Pan, T.J. Rupert, Physical Review B, 93 (2016) 134113.

[28] T. Frolov, M. Asta, Y. Mishin, Physical Review B, 92 (2015) 020103.

[29] S.J. Dillon, M.P. Harmer, J. Luo, JOM, 61 (2009) 38-44.

[30] E. Ma, Scripta Materialia, 49 (2003) 663-668.

[31] A. Khalajhedayati, Z. Pan, T.J. Rupert, Nature Communications, 7 (2016).

[32] M. Tang, W.C. Carter, R.M. Cannon, Physical Review B, 73 (2006) 024102.

[33] J. Luo, X. Shi, Applied Physics Letters, 92 (2008) 101901.

[34] J.E. Ludy, T.J. Rupert, Scripta Materialia, 110 (2016) 37-40.

[35] K.L. Murty, I. Charit, Journal of Nuclear Materials, 383 (2008) 189-195.

[36] A. Van Veen, J. Evans, L. Caspers, J.T.M. De Hosson, Journal of Nuclear Materials, 122 (1984) 560-564.

[37] J. Evans, A. Van Veen, J.T.M. De Hosson, R. Bullough, J. Willis, Journal of Nuclear Materials, 125 (1984) 298-303.

[38] W. Han, M.J. Demkowicz, N.A. Mara, E. Fu, S. Sinha, A.D. Rollett, Y. Wang, J.S. Carpenter, I.J. Beyerlein, A. Misra, Advanced Materials, 25 (2013) 6975-6979.

[39] E. Fu, J. Carter, G. Swadener, A. Misra, L. Shao, H. Wang, X. Zhang, Journal of nuclear materials, 385 (2009) 629-632.

[40] N. Nita*, R. Schaeublin, M. Victoria, R. Valiev, Philosophical Magazine, 85 (2005) 723-735.

[41] M. Demkowicz, P. Bellon, B. Wirth, MRS Bulletin, 35 (2010) 992-998.

[42] A.R. Yavari, A. Le Moulec, A. Inoue, N. Nishiyama, N. Lupu, E. Matsubara, W.J. Botta, G. Vaughan, M. Di Michiel, Å. Kvick, Acta Materialia, 53 (2005) 1611-1619.

[43] Y. Wang, J. Li, A.V. Hamza, T.W. Barbee, Proceedings of the National Academy of Sciences, 104 (2007) 11155-11160.

[44] D. Raabe, M. Herbig, S. Sandlöbes, Y. Li, D. Tytko, M. Kuzmina, D. Ponge, P.-P. Choi, Current Opinion in Solid State and Materials Science, 18 (2014) 253-261.

[45] X. Shi, J. Luo, Physical Review B, 84 (2011) 014105.

[46] W. Phythian, R. Stoller, A. Foreman, A. Calder, D. Bacon, Journal of Nuclear Materials, 223 (1995) 245-261.

[47] M. Mendelev, M. Kramer, R. Ott, D. Sordelet, D. Yagodin, P. Popel, Philosophical Magazine, 89 (2009) 967-987.

[48] M. Mendelev, D. Sordelet, M. Kramer, Journal of Applied Physics, 102 (2007) 043501.

[49] M. Demkowicz, R. Hoagland, International Journal of Applied Mechanics, 1 (2009) 421-442.

[50] C.H. Rycroft, Chaos, 19 (2009) 041111.

[51] M. Caturla, N. Soneda, E. Alonso, B. Wirth, T.D. de la Rubia, J. Perlado, Journal of Nuclear Materials, 276 (2000) 13-21.

[52] A. Slipenyuk, J. Eckert, Scripta Materialia, 50 (2004) 39-44.

[53] D.B. Miracle, Nature materials, 3 (2004) 697-702.

[54] E. Ma, Nature Materials, 14 (2015) 547-552.

[55] R. Kirchheim, Acta Materialia, 55 (2007) 5129-5138.

[56] G. Gottstein, L.S. Shvindlerman, Grain boundary migration in metals: thermodynamics, kinetics, applications, CRC press, 2009.

[57] J. Luo, H. Wang, Y.-M. Chiang, Journal of the American Ceramic Society, 82 (1999) 916-920.

[58] J. Luo, V.K. Gupta, D.H. Yoon, H.M. Meyer, Applied Physics Letters, 87 (2005) 231902.
[59] J. Luo, Current Opinion in Solid State and Materials Science, 12 (2008) 81-88.

[60] Z. Pan, T.J. Rupert, Acta Materialia, 89 (2015) 205-214.

[61] P.F. Becher, G.S. Painter, E.Y. Sun, C.H. Hsueh, M.J. Lance, Acta Materialia, 48 (2000) 4493-4499.

[62] P.L. Williams, Y. Mishin, Acta Materialia, 57 (2009) 3786-3794.

[63] D.A. Litton, S.H. Garofalini, Journal of the American Ceramic Society, 83 (2000) 2273-2281.

[64] D. Raabe, S. Ohsaki, K. Hono, Acta Materialia, 57 (2009) 5254-5263.

[65] W.H. Wang, C. Dong, C.H. Shek, Materials Science and Engineering: R: Reports, 44 (2004) 45-89.

[66] Z. Liang, M. Enrique, C. Alfredo, L. Xiang-Yang, J.D. Michael, Modelling and Simulation in Materials Science and Engineering, 21 (2013) 025005.

[67] B. Sadigh, P. Erhart, A. Stukowski, A. Caro, E. Martinez, L. Zepeda-Ruiz, Physical Review B, 85 (2012) 184203.

[68] D.J. Chakrabarti, D.E. Laughlin, Bulletin of Alloy Phase Diagrams, 2 (1982) 455-460.

[69] Y. Zhang, J. Luo, Scripta Materialia, 88 (2014) 45-48.

[70] P. Wynblatt, D. Chatain, Metallurgical and Materials Transactions A, 37 (2006) 2595-2620.